The Astrophysical Journal, 880:136 (13pp), 2019 August 1 https://doi.org/10.3847/1538-4357/ab2764

The Role of Energy Diffusion in the Deposition of Energetic Electron Energy in Solar and Stellar Flares

Natasha L. S. Jeffrey, Eduard P. Kontar, and Lyndsay Fletcher
School of Physics & Astronomy, University of Glasgow, G12 8QQ, Glasgow, UK; natasha.jeffrey@glasgow.ac.uk
Received 2019 April 4; revised 2019 May 20; accepted 2019 June 4; published 2019 August 2

Abstract

During solar flares, a large fraction of the released magnetic energy is carried by energetic electrons that transfer and deposit energy in the Sun's atmosphere. Electron transport is often approximated by a cold thick-target model, assuming that electron energy is much larger than the temperature of the ambient plasma, and electron energy evolution is modeled as a systematic loss. Using kinetic modeling of electrons, we reevaluate the transport and deposition of flare energy. Using a full collisional warm-target model (WTM), we account for electron thermalization and for the properties of the ambient coronal plasma such as its number density, temperature and spatial extent. We show that the deposition of nonthermal electron energy in the lower atmosphere is highly dependent on the properties of the flaring coronal plasma. In general, thermalization and a reduced WTM energy loss rate leads to an increase of nonthermal energy transferred to the chromosphere, and the deposition of nonthermal energy at greater depths. The simulations show that energy is deposited in the lower atmosphere initially by high-energy nonthermal electrons, and later by lower energy nonthermal electrons that partially or fully thermalize in the corona, over timescales of seconds, unaccounted for in previous studies. This delayed heating may act as a diagnostic of both the injected nonthermal electron distribution and the coronal plasma, vital for constraining flare energetics.

Key words: stars: flare – Sun: atmosphere – Sun: chromosphere – Sun: corona – Sun: flares – Sun: X-rays, gamma rays

1. Introduction

Solar flares are a product of the Sun's magnetic energy being released and then ultimately dissipated in different layers of its vast atmosphere. The release of magnetic energy, initiated by magnetic reconnection in the corona (e.g., Parker 1957; Sweet 1958; Priest & Forbes 2000), is partitioned into thermal and nonthermal particle energies (e.g., Emslie et al. 2012; Aschwanden et al. 2015, 2017; Warmuth & Mann 2016), and kinetic plasma motions ("turbulence"), a vital energy transfer mechanism in the process (e.g., Larosa & Moore 1993; Petrosian 2012; Vlahos et al. 2016; Kontar et al. 2017). However, the bulk of the released energy is eventually transferred to the Sun's cool and dense low atmosphere (the chromosphere) causing rapid heating, ionization (see Fletcher et al. 2011; Holman et al. 2011), and an expansion of the lower atmospheric material—"chromospheric evaporation" (e.g., Sturrock 1973; Hirayama 1974; Acton et al. 1982; Holman et al. 2011). The heated chromosphere, a thin and complex layer, is a prime source of deposited energy information, mainly radiating in optical and ultraviolet wavelengths (e.g., Hirayama 1974; Woods et al. 2006; Kretzschmar 2011). Energy is likely transferred in a variety of different, but closely connected, ways, by flare-accelerated electrons, as evident from hard X-ray (HXR) observations (Holman et al. 2011), by thermal conduction (e.g., Culhane et al. 1970), and complicated by various plasma waves e.g., acoustic waves (e.g., Vlahos & Papadopoulos 1979), Alfvén waves (e.g., Emslie & Sturrock 1982; Fletcher & Hudson 2008), Langmuir waves (Emslie & Smith 1984; McClements 1987; Hannah et al. 2009), whistler waves (e.g., Bespalov et al. 1991; Stepanov et al. 2007), and then dissipated via turbulence, even in the lower atmosphere e.g., Jeffrey et al. (2018).

In the flare impulsive phase, X-ray observations (Benz 2008; Kontar et al. 2011a) suggest that nonthermal electrons are the main source of low atmosphere heating and radiation. Bremsstrahlung X-rays provide a relatively direct diagnostic of the properties of flare-accelerated electrons (see Kontar et al. 2011a) in the corona and in the dense lower atmosphere via HXR footpoints (e.g., Hoyng et al. 1981). Higher energy HXRs are observed to be produced in progressively lower regions of the chromosphere (Aschwanden et al. 2002; Kontar et al. 2010) by electron–ion (mainly proton) collisions, and via electron–electron collisions above ∼300 keV (Kontar et al. 2007). However, electrons predominantly exchange energy via electron–electron collisions (see Holman et al. 2011). Flare observations of "coronal thick-target" sources (e.g., Aschwanden et al. 1997; Veronig & Brown 2004; Xu et al. 2008; Kontar et al. 2011b; Guo et al. 2012; Jeffrey & Kontar 2013) show that electrons with energies up to ≈30 keV can thermalize in the corona in high density conditions. However, more general statistical studies of large flares (e.g., Caspi et al. 2014; Aschwanden et al. 2015) show that the flaring corona, at least within the main phase, is often a highly collisional environment. Further, it is likely that noncollisional transport effects such as turbulent scattering by magnetic fluctuations (Bespalov et al. 1991; Kontar et al. 2014), beam-driven Langmuir wave turbulence (Hannah et al. 2009), electron reacceleration (Brown et al. 2009) and/or beam-driven return current (Knight & Sturrock 1977; Emslie 1980; Zharkova & Gordovskyy 2006; Alaoui & Holman 2017) are also operating during flares, complicating the overall transport.

For the last fifty years, the properties of nonthermal electrons (their transport, deposition, and the heating of the lower atmosphere), are often determined using the "cold-thick-target" collisional transport model (hereafter CTTM; e.g., Brown 1971;

Syrovatskii & Shmeleva 1972; Emslie 1978). The CTTM assumes that the energy E of nonthermal electrons is much larger than the ambient plasma temperature T, and hence "cold" (i.e., $T \ll E$). Although this assumption is valid for high-energy electrons that reach the cool layers of the flaring chromosphere, decades of observational evidence with e.g., Yohkoh (Tsuneta et al. 1991) and the *Reuven Ramaty High Energy Solar Spectroscopic Imager* (*RHESSI*; Lin et al. 2002) show high coronal temperatures of 10–30 MK during flares. However, the lasting appeal of the CTTM is its simple analytic form, that can be readily applied to X-ray data, but its use leads to the well-known "low-energy cutoff" problem, whereby the power associated with nonthermal electrons cannot be constrained from X-ray spectroscopy. First, Jeffrey et al. (2014), building upon Emslie (2003) and Galloway et al. (2005), studied electron transport using a full collisional model including finite temperature effects, diffusion and pitch-angle scattering, and showed the importance of including the properties of the coronal plasma (its finite temperature, density, and extent). Critically, the inclusion of both thermalization and spatial diffusion led to the "warm-target model" (hereafter WTM; derived by Kontar et al. 2015) that can resolve the problems associated with determining the low-energy cutoff in the CTTM, finally allowing the power of flare-accelerated electrons to be constrained (Kontar et al. 2019) from X-ray data. In a WTM, the properties and energy content of nonthermal electrons are constrained by determining the plasma properties of the flaring corona.

Here, using full collisional kinetic modeling, we reinvestigate flare-accelerated electron energy deposition. As expected, we show that the coronal plasma properties (e.g., temperature, number density, and spatial extent) determine how nonthermal electron power is deposited in the chromosphere. Ultimately, we show for a given nonthermal electron distribution, a greater proportion of the nonthermal electron power can be deposited in the lower atmosphere than predicted in the CTTM.

2. Electron Transport and Deposition in Hot Collisional Plasma

To determine how the energy of flare-accelerated electrons is transported and deposited in a hot collisional plasma (i.e., in a full collisional WTM), we use the kinetic electron transport simulation first discussed in Jeffrey et al. (2014) and Kontar et al. (2015). We model the evolution of an electron flux $F(z, E, \mu)$ (electron $\mathrm{erg}^{-1}\,\mathrm{s}^{-1}\,\mathrm{cm}^{-2}$) in space z (cm), energy E (erg), and pitch-angle μ to a guiding magnetic field, using the Fokker–Planck equation of the form (e.g., Lifshitz & Pitaevskii 1981; Karney 1986)

$$\mu\frac{\partial F}{\partial z} = \Gamma m_e^2\left(\frac{\partial}{\partial E}\left[G(u[E])\frac{\partial F}{\partial E} + \frac{G(u[E])}{E}\left(\frac{E}{k_{\mathrm{B}}T} - 1\right)F\right]\right) + \Gamma m_e^2\left(\frac{1}{8E^2}\frac{\partial}{\partial \mu}\left[(1-\mu^2)(\mathrm{erf}(u[E]) - G(u[E]))\frac{\partial F}{\partial \mu}\right]\right) + S(E, z, \mu), \quad (1)$$

where $\Gamma = 4\pi e^4 \ln\Lambda\, n/m_e^2 = 2Kn/m_e^2$, and e (esu) is the electron charge, n is the plasma number density (cm^{-3}) (a hydrogen plasma is assumed), m_e is the electron rest mass (g), and $\ln\Lambda$ is the Coulomb logarithm. The variable $u(E) = \sqrt{E/k_{\mathrm{B}}T}$, where k_{B} ($\mathrm{erg\,K}^{-1}$) is the Boltzmann constant and T (K) is the background plasma temperature. The functions $\mathrm{erf}(u)$ (the error function) and $G(u)$ are given by

$$\mathrm{erf}(u) \equiv (2/\sqrt{\pi})\int_0^u \exp(-t^2)\,dt \quad (2)$$

and

$$G(u) = \frac{\mathrm{erf}(u) - u\,\mathrm{erf}'(u)}{2u^2}. \quad (3)$$

Equation (1) is a time-independent equation useful for studying solar flares where the electron transport time from the corona to the lower atmosphere is usually shorter than the observational time (i.e., most X-ray observations have integration times of tens of seconds to minutes).

Here, Equation (1) models electron–electron collisions only, the dominant electron energy loss mechanism in the flaring plasma.[1] $S(E, z, \mu)$ plays the role of the electron flux source function and the properties of the injected electron distribution are discussed in Section 2.3.

Following Jeffrey et al. (2014), and rewriting Equation (1) as a Kolmogorov forward equation (Kolmogorov 1931), Equation (1) can be converted to a set of time-independent stochastic differential equations (e.g., Gardiner 1986; Strauss & Effenberger 2017) that describe the evolution of z, E, and μ in Itô calculus:

$$z_{j+1} = z_j + \mu_j\,\Delta s; \quad (4)$$

$$E_{j+1} = E_j - \frac{\Gamma m_e^2}{2E_j}(\mathrm{erf}(u_j) - 2u_j\,\mathrm{erf}'(u_j))\,\Delta s + \sqrt{2\,\Gamma m_e^2\,G(u_j)\,\Delta s}\;W_E; \quad (5)$$

$$\mu_{j+1} = \mu_j - \frac{\Gamma m_e^2(\mathrm{erf}(u_j) - G(u_j))}{4E_j^2}\mu_j\,\Delta s + \sqrt{\frac{(1-\mu_j^2)\,\Gamma m_e^2(\mathrm{erf}(u_j) - G(u_j))}{4E_j^2}\Delta s}\;W_\mu. \quad (6)$$

Δs (cm) is the step size along the particle path, and W_μ, W_E are random numbers drawn from Gaussian distributions with zero mean and a unit variance representing the corresponding Wiener processes (e.g., Gardiner 1986). A simulation step size of $\Delta s = 10^5$ cm is used in all simulations, and E, μ, and z are updated at each step j. A step size of $\Delta s = 10^5$ cm is approximately two orders of magnitude smaller than the thermal collisional length in a dense ($n = 10^{11}\,\mathrm{cm}^{-3}$) plasma with $T \geqslant 10$ MK (or the collisional length of an electron with an energy of 1 keV or greater, in a cold plasma). The simulation ends when all "electrons" have left the warm-target corona, and reached the cool "chromosphere" (where a CTTM approximation is valid for all studied energies). Using a time-independent equation with a constant source of injection produces output variables with units of (electron s^{-1} per output variable) i.e., E, z, or μ, and the final results are reconstructed by summing over all outputs at each step j. The derivation of Equation (1) and the detailed description of the simulations can be found in Jeffrey et al. (2014).

[1] We note that electron–proton interactions are important for collisional pitch-angle scattering, but here we only model electron–electron interactions. Equation (1) can be generalized to model any particle–particle collisions.

Equation (1) (and Equations (5) and (6)) diverge as $E \rightarrow 0$, and as discussed in Jeffrey et al. (2014), the deterministic equation $E_{j+1} = \left[E_j^{3/2} + \frac{3\Gamma m_e^2}{2\sqrt{\pi k_B T}}\Delta s\right]$ must be used for low energies where $E_j \leqslant E_{\rm low}$ using $E_{\rm low} = \left[\frac{3\Gamma m_e^2}{2\sqrt{\pi k_B T}\Delta s}\right]^{2/3}$—see Jeffrey et al. (2014), following Lemons et al. (2009). For such low-energy thermal electrons, μ_{j+1} can be drawn from an isotropic distribution $\mu \in [-1, +1]$.

2.1. The Deposition of Nonthermal Electron Power

Electron energy deposited into the ambient plasma can be determined by considering

$$\Delta E_{j+1}(z) = E_j(z) - E_{j+1}(z), \tag{7}$$

where E_j and E_{j+1} are the electron energies before and after each simulation step, respectively. Using $\Delta E_{j+1}(z)$, a new ambient background temperature at that location can also be determined. However, we do not examine changes in background plasma temperature, and the background temperature remains constant in all simulations.

Although derived from a time-independent equation, we note that Equations (4)–(6) are related to a time step Δt by $\Delta t = \Delta s/v$, where $v = \sqrt{2E/m_e}$ is the velocity of the electron, and the simulations can also be used for a time-dependent analysis. In all simulations, the total time it takes for an electron to deposit all of its energy can be approximated using

$$t = \sum_j \frac{|z_{j+1} - z_j|}{\sqrt{2E_j/m_e}}. \tag{8}$$

In cases where $\mu_j \approx 0$, we use $|z_{j+1} - z_j| \approx \Delta s$. Also in the CTTM, this time can be estimated analytically using $t = \frac{E_0^2}{2Knv}$, where E_0 is the injected energy of the electron.

During each simulation step j, in order to determine the nonthermal electron power $P_{j+1}(z)$ at each spatial location z, we weight the output of (electron $\rm s^{-1}\,cm^{-1}$) in each z bin by the total ΔE_{j+1} deposited in that bin, giving $P_{j+1}(z)$ (erg $\rm s^{-1}\,cm^{-1}$). Summing over all saved j gives the total nonthermal electron power $P(z)$ deposited at each spatial location z, equivalent to

$$P(z) = \int_0^\infty EF(E, z)dE. \tag{9}$$

Further, summing over all z gives the total spatially integrated nonthermal electron power (erg $\rm s^{-1}$), which can be compared with the injected nonthermal electron power P (erg $\rm s^{-1}$) input into the simulation. For an injected nonthermal electron power-law distribution (see Holman et al. 2011), this can be written as

$$P = \int_{E_c}^\infty E_0 F(E_0)dE_0 = \dot{N}_0 E_c \frac{(\delta - 1)}{(\delta - 2)}, \tag{10}$$

for the injected energies E_0, an acceleration rate $\dot{N}_0$ (electron $\rm s^{-1}$), a low-energy cutoff of E_c (the lowest energy in the nonthermal electron distribution), and the power-law spectral index δ.

2.2. Flare Plasma Parameters

We model the flaring atmosphere using a hot-corona–cool-chromosphere type model (see Figures 1 and 2). This atmosphere is a simple but reasonable description of most flaring atmospheres. Moreover, a more realistic atmosphere is not required since we only want to compare the results of the CTTM and WTM. This type of atmosphere also ensures that a time-independent stationary solution is reached (e.g., see Kontar et al. 2015, for details). Unlike the CTTM, electrons are no longer lost energetically, but accumulate in the corona as they thermalize. This pile-up of thermalized electrons in the corona is balanced by the spatial diffusion of electrons from the hot corona into the cool chromosphere, which can be still considered a cold-target.

We perform simulation runs for two different "hot corona–cool chromosphere" model atmospheres (see Figure 2), including one model that includes a chromosphere with an exponential density profile (e.g., Vernazza et al. 1981; Battaglia et al. 2012).

The development of the WTM has shown that the plasma parameters (the coronal temperature T, the coronal number density n, and the coronal plasma extent L, where the temperature is high enough to be visible in X-rays) are crucial for determining and constraining the properties of flare-accelerated electrons (Kontar et al. 2019). Here, we show how the plasma properties play a key role in the transfer and the deposition of nonthermal electron power. We test how the energy of nonthermal electrons is transferred and deposited in a range of different coronal plasma conditions. In the corona, we use different number densities ranging from $n = 3 \times 10^{10}\,\rm cm^{-3}$ to $n = 1 \times 10^{11}\,\rm cm^{-3}$, and plasma extents (half-loop lengths L) of either $20''$ or $30''$ (see Figure 1) between the hot corona and cooler chromosphere, leading to column depths of 10^{19}–$10^{20}\,\rm cm^{-2}$. In the WTM cases, coronal temperatures range from 10 to 30 MK (see Figure 1) for solar/M-dwarf cases and up to 100 MK for comparison with certain extreme stellar cases (e.g., see Figure 3 in Aschwanden et al. 2008). In atmosphere type 1, in the cool "chromosphere type" region, the number density rises to $n = 1 \times 10^{12}\,\rm cm^{-3}$ and the temperature falls to $T \sim 0$ MK, i.e., it is approximated as a CTTM. In the more realistic atmosphere type 2, the density at the boundary of the cool "chromosphere type" region is set at $n = 1 \times 10^{12}\,\rm cm^{-3}$, but this rises quickly to photospheric densities of $n = \sim 10^{17}\,\rm cm^{-3}$ over $\sim 3''$ using

$$n = 10^{12}\,(\rm cm^{-3}) + n_{\rm photo}\exp\left(-\frac{|z| + 23\farcs5}{h_0}\right), \tag{11}$$

where $n_{\rm photo} = 1.16 \times 10^{17}\,\rm cm^{-3}$ is the photospheric density at the optical depth of ≈ 1, and here z is measured in arcseconds. The scale height h_0 of the density profile is set at $0\farcs18 \sim 130$ km (e.g., following the simulations of Battaglia et al. 2012).

In most solar flare coronal conditions, $\ln \Lambda \approx 20$, but we can calculate $\ln \Lambda$ using (e.g., Somov 2007),

$$\ln \Lambda = \ln\left[\frac{3}{2e^3}\left(\frac{k_B^3 T^3}{\pi n}\right)^{1/2}\right]. \tag{12}$$

In the CTTM simulations, we choose $T = T_{\rm corona}$, where $T_{\rm corona}$ is the background corona temperature used in the WTM simulations. In the lower "cold-target" atmosphere, we choose $T = 0.01$ MK for the calculation of $\ln \Lambda$.

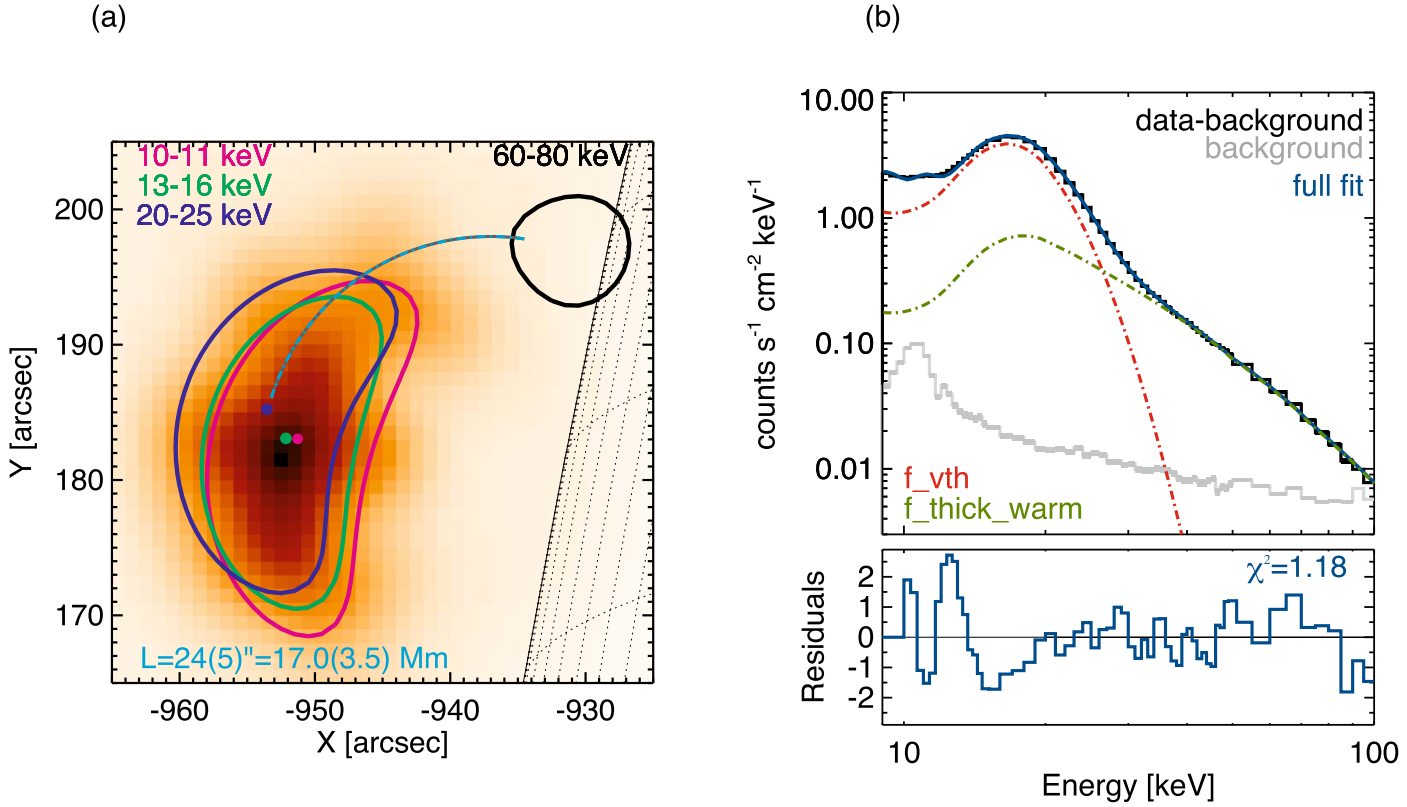

Figure 1. A *RHESSI* X-ray observation of a flare (SOL2013-05-13T02:12). (a) We observe lower energy X-rays from a hot thermal source in the corona and higher energy X-rays from accelerated electrons reaching the cooler and denser chromosphere. (b) The total spatially integrated X-ray count spectrum fitted with a thermal component (red) and a WTM component (green) that accounts for both high-energy electrons (power law) and low-energy thermalized electrons. From combined X-ray spectroscopy and imaging, we determine that the coronal source is hot and dense with $\langle T \rangle \approx 29$ MK and $\langle n \rangle \approx 9 \times 10^{10}$ cm^{-3}. Here, the distance between the X-ray coronal and footpoint sources is $L \approx 24''$. The determination of these coronal plasma properties is vital for constraining electron transport and deposition. Figures taken from Kontar et al. (2019).

2.3. The Injected Electron Distribution

The source function $S(E, z, \mu)$ is made up of three separate distributions:

1. Injected energy spectrum—we input either a monoenergetic distribution or a power-law distribution of the form $\sim E_0^{-\delta}$. Electron distributions with approximate power-law forms are routinely observed via X-ray observations. In the monoenergetic cases, we input electrons with coronal thermal 10, 20, 30, 40, 50, or 100 keV energies. In these cases, we compare the outputs using $\dot{N}_0 = 1\,\mathrm{s}^{-1}$. For the power-law case, parameters of $\delta = 4$ or $\delta = 7$, a low-energy cutoff of $E_c = 10$ keV or $E_c = 20$ keV, and a high-energy cutoff of $E_H = 50$ keV are used.[2] In power-law cases, the electron injection rate $\dot{N}_0$ is set at a value that gives the total injected electron power $P = 4.8 \times 10^{27}$ erg s^{-1}.
2. Injected pitch-angle distribution—we input a beamed distribution (with half moving in one direction and half moving in the opposite direction, i.e., $\mu = +1$ or $\mu = -1$). We also run simulations using a completely isotropic distribution ($\mu \in [-1, +1]$), but for brevity the results are not shown here. In general, the injected pitch-angle distribution is not well-constrained by current solar flare observations (e.g., Kontar et al. 2011a; Casadei et al. 2017). Collisional (electron–electron only) pitch-angle scattering is always modeled in the simulations. Further, it is very likely that other noncollisional (and shorter timescale) turbulent scattering mechanisms are also present in the flaring atmosphere (Kontar et al. 2014). This will also change how the electron energy is deposited spatially and temporally, and the subject of ongoing work.
3. Injected spatial distribution—we input the electrons as a Gaussian distribution centered at the loop top apex ($z = 0''$), with a standard deviation of $1''$. It is possible that electrons are accelerated to varying levels (dependent on the plasma conditions) at multiple points along a twisted loop (e.g., Gordovskyy & Browning 2012; Gordovskyy et al. 2014), but again simulating all possible cases is beyond the scope of the paper and it is not required for a CTTM and WTM comparison.

[2] Electrons with energies above ~50 keV will approximate the CTTM solution using the noted plasma parameters, and low-energy electrons carry the bulk of the power due to steeply decreasing power laws.

2.4. Timescales for the Deposition of Nonthermal Electron Power

Unlike the CTTM case, in a WTM, electrons "stopped" in the coronal plasma thermalize and then diffuse through the coronal region in a random walk, continuously exchanging energy with the background population. Ultimately, this means that nonthermal electrons fully thermalized in the hot corona still transfer some fraction of their injected energy to the cool lower atmosphere (see the cartoon in Figure 3(i)).

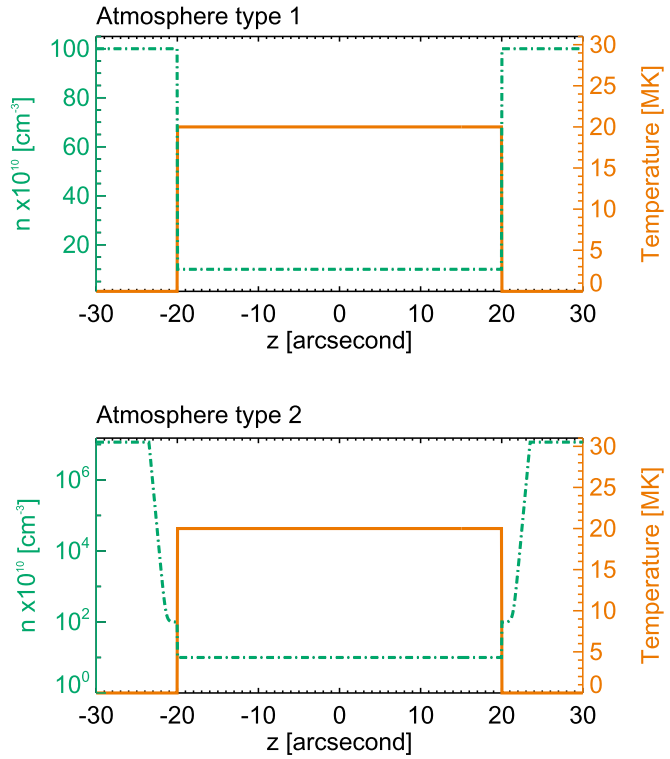

Figure 2. The different atmospheric types used in the simulations. Top: Atmosphere 1—a constant coronal temperature (we use either 10, 20, 30, or 100 MK) and number density (either 3×10^{10}, 7×10^{10}, or 1×10^{11} cm^{-3}) and "cold-target" chromosphere with $n = 10^{12}$ cm^{-3}. Bottom: Atmosphere 2—as Atmosphere 1 with a constant coronal temperature and number density, but with an exponentially increasing chromospheric density (see Section 2.2), with a scale height of 130 km and photospheric density of $n_{\rm photo} = 1.16 \times 10^{17}$ cm^{-3}. The coronal plasma has a half-loop length of either $L = 20''$ or $L = 30''$.

Moreover, the time is takes for an injected thermal electron, which is dominated by diffusion, to leave the corona and deposit its energy in a cool low atmosphere (cold-target) can be estimated analytically using

$$\tau_D = \sqrt{\frac{8m_e}{\pi}}\ \frac{KnL^2}{3}(k_{\rm B}T)^{-5/2}, \tag{13}$$

where $K = 2\pi\ e^4\ \ln\Lambda$. This diffusion time ($\tau_D$; Equation (13)) is comparable to the Spitzer thermal conduction time (Spitzer 1962). In Figure 3(ii), we calculate τ_D for a range of different coronal parameters (T, n, and L). τ_D increases with increasing n and L, and decreases with increasing T (thermalized electrons in hotter plasma have a higher thermal energy and hence reach the chromosphere quicker). For the range of plasma parameters used in the simulations, τ_D ranges between ~1 and 100 s. Although, the thermal electron diffusion time τ_D can be calculated analytically, it is not trivial to determine the deposition timescales for nonthermal electrons injected with $E > k_{\rm B}T$ into different coronal plasma conditions. Therefore, in each simulation run, we determine the time it takes for nonthermal electrons of different injected energies to deposit their energy in the lower atmosphere using Equation (8).

In these simulations, we stress that we do not consider the energy transferred from the hot corona to the cool lower atmosphere from the background thermal plasma by thermal conduction, which will play a varying role in different flares and at different stages as the flare progresses. Here, we only consider the energy transferred by nonthermal electrons, and in particular, the "extra" component of energy that comes from partially or fully thermalized nonthermal electrons now being able to reach the lower atmosphere from diffusion.

In the simulations, we make several simplifying assumptions, such as: (1) use of single temperature and number density in the corona, (2) a previously heated corona and the use of a coronal "thermal bath" approximation, i.e., there are no significant changes in the background energy content due to the transport and deposition of nonthermal electron energy, and (3) the use of a "step function" type atmosphere. Here, the assumptions are valid for a CTTM and WTM comparison, as stated. Further, the thermal diffusion of electrons is a fundamental transport mechanism always present in flares (to a varying degree depending on the coronal environment), that is usually overlooked, even in Fokker–Planck type simulations where a full collisional model is used. Hence, more complex simulations are not required here, and they would hinder our comparison of energy transport in the CTTM and WTM, which is the main aim of this study.

3. Simulation Results

3.1. Monoenergetic Energy Inputs: Spatial Distribution of Deposited Power

First, we perform simulations where we input different monoenergetic electron distributions into different plasma environments, so that the results of the WTM and CTTM can be easily compared for electrons of different energies in a range of different coronal conditions. Here, in each simulation run, the accelerated electron rate is $\dot{N}_0 = 1\,{\rm s}^{-1}$, for each input. We perform four different sets of simulations labeled (a)–(d), using atmosphere 1 (see Figure 2):

Sets (a) and (b)—different coronal densities: in sets (a) and (b), we input monoenergetic electrons with energies of either 10, 20, 30, 40, 50, or 100 keV. The injected electrons are initially beamed in μ, and spread in z as a Gaussian with a $1''$ standard deviation centered at the loop apex. They are injected into atmosphere type 1 (see Figure 2), with either a coronal density of (a) $n = 10^{11}$ cm^{-3} (Figure 4), or (b) $n = 3 \times 10^{10}$ cm^{-3} (Figure 5), a half-loop length of $L = 20''$, and for all the WTM cases, a coronal temperature of $T = 20$ MK (giving $E/k_{\rm B}T = 5.8$, 11.6, 17.4, 23.2, 29.0, 57.9). All the WTM and CTTM results are shown in Figures 4 and 5 (showing the spatial distribution of nonthermal power deposition in units of keV s^{-1} arcsec^{-1} and the ratio of the WTM to CTTM result for each run). Tables 1 and 2 show the percentage of nonthermal power deposited in the corona or low atmosphere in both WTM and CTTM cases. From the results of (a) and (b) we find:

1. In (a) and (b), the spatial distribution of deposition in the WTM is different from the CTTM for all energies up to and including ≈50 keV, and this difference increases for larger coronal densities and smaller injected electron energies (see Figures 4 and 5).
2. In (a) and (b), electrons can move further and deposit more energy at greater depths in both the corona and low atmosphere in the WTM. This is most obvious for low-energy electrons (<30 keV) in a high density corona. Such electrons are collisionally stopped in the corona. The CTTM predicts that they deposit all of their energy in

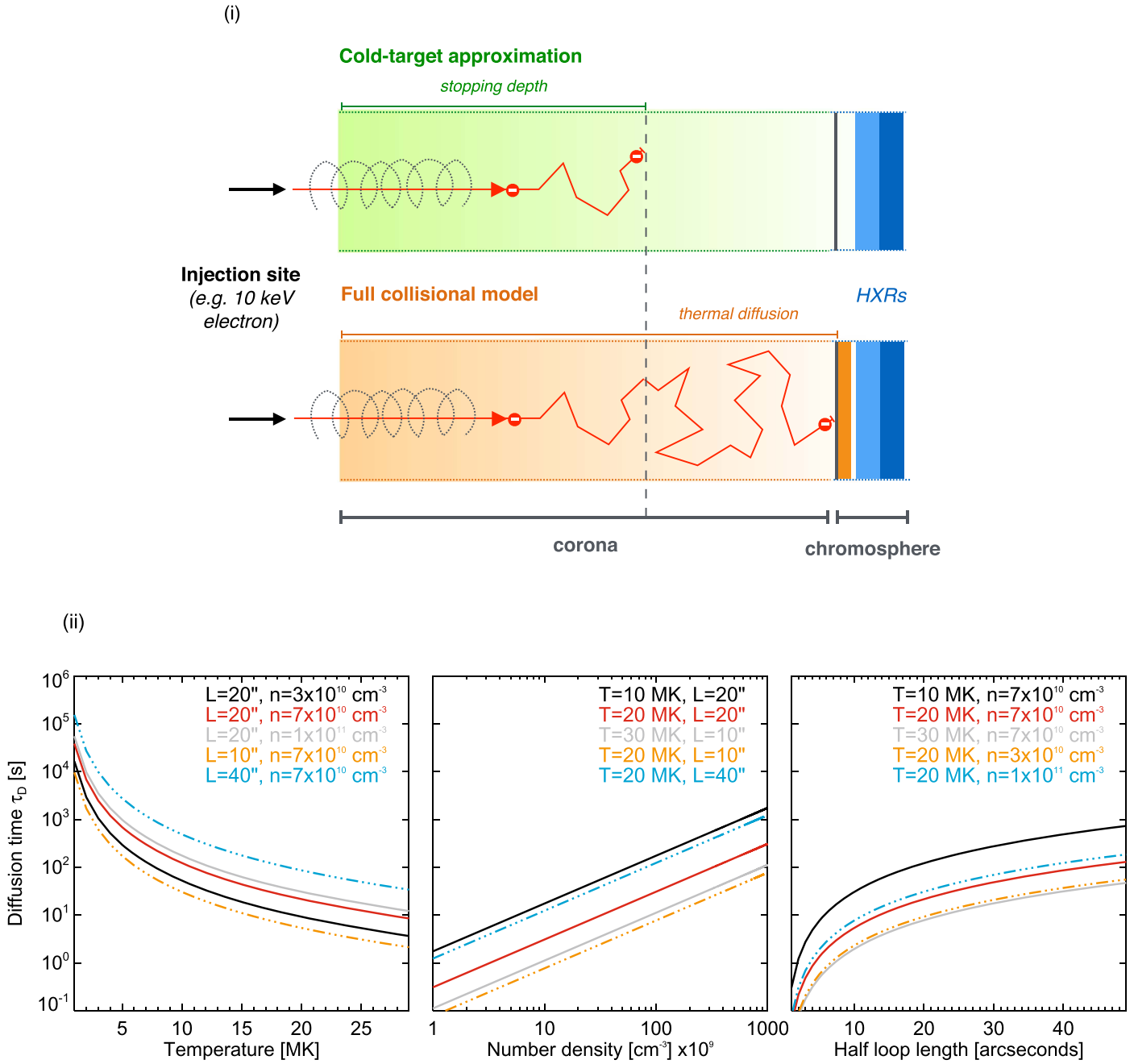

Figure 3. (i) Cartoon showing the difference between low-energy electron transport in a CTTM and full collisional model (WTM). In a CTTM, low-energy electrons might never reach the chromosphere if they are collisionally stopped in the corona, but in a WTM, such electrons are thermalized and can still transport a fraction of their nonthermal energy from the hot corona to the cool chromosphere via thermal diffusion (orange layer in the chromosphere). (ii) Comparison of the time it takes a thermalized electron to spatially diffuse from a hot coronal source to a cooler and denser low atmosphere, using different coronal plasma conditions of number density n, temperature T, and the distance between the coronal source and the chromosphere L. For solar flare conditions, i.e., $T \approx 10$–30 MK, $n \approx 10^{10}$–10^{11} cm^{-3}, and $L \approx 20''$–$30''$, τ_D ranges between 1 and 100 s. Such timescales are important in the WTM where nonthermal electrons partially or fully thermalize during their transport in the corona and hence transfer energy to the chromosphere on timescales of seconds.

the corona. In the WTM, electrons thermalize (or tend toward a Maxwellian) and eventually deposit some fraction of their original energy content in the low atmosphere (see Tables 1 and 2 for a comparison of the CTTM and WTM percentages). For example, in (a), an injected 20 keV electron population now deposits ∼20% of its available nonthermal power in the lower atmosphere, compared to 0% in a CTTM.

3. The ratio of WTM to CTTM deposition is an informative parameter that shows, in a single given location, up to 100 times more nonthermal electron power can be deposited (in both the corona and low atmosphere), than predicted by the CTTM, for a given injection of nonthermal electrons (see Figures 4 and 5).

Set (c)—different coronal temperatures: in set (c), we compare WTM and CTTM deposition in different coronal plasma temperatures of $T = 10$, 20, 30, 100 MK. We inject initially beamed, monoenergetic electrons with an energy of 30 keV only (giving $E/k_BT = 34.8$, 17.4, 11.6, 3.5), into

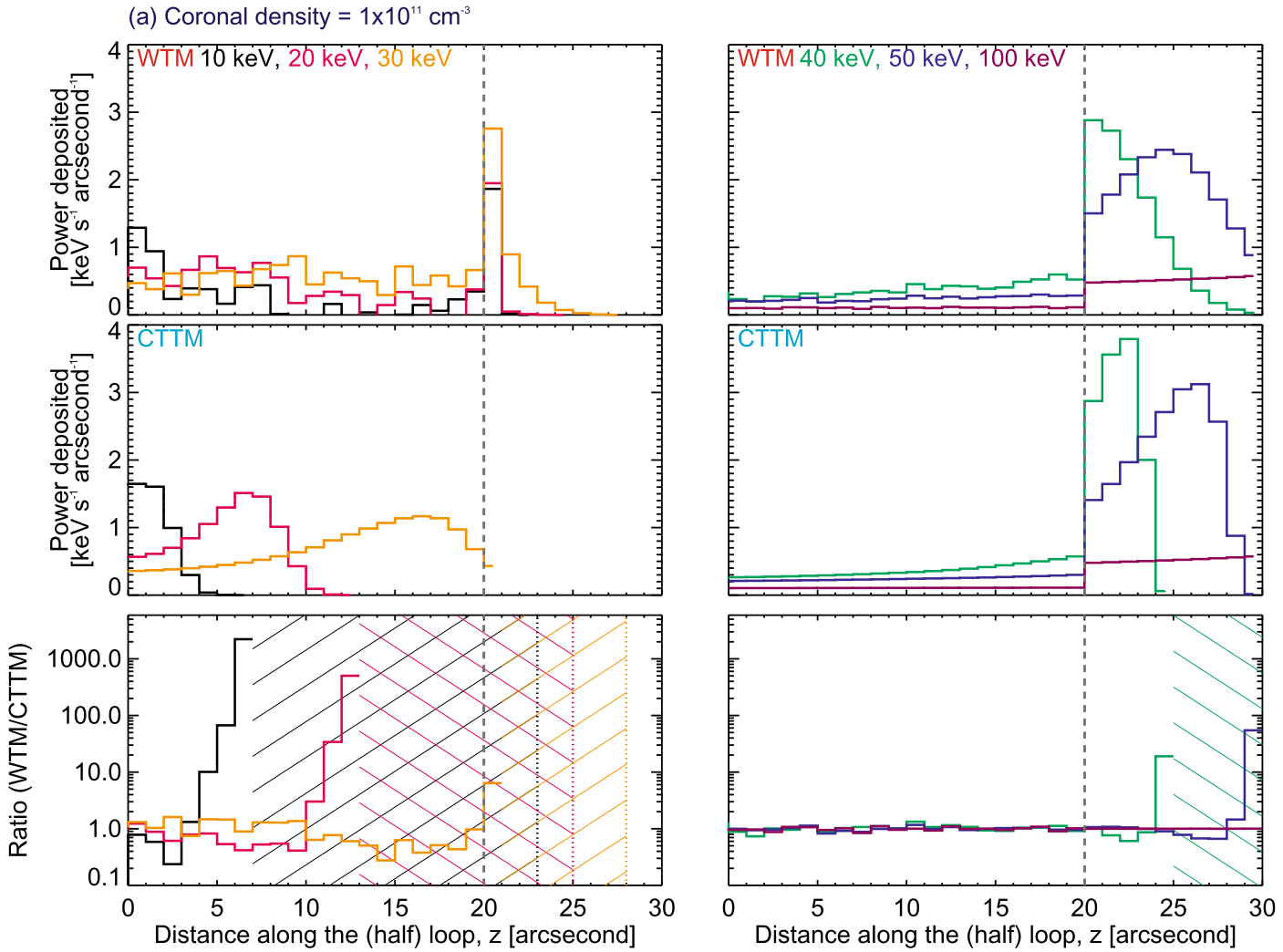

Figure 4. High density flaring corona. The results for the (initially) monoenergetic simulation set (a) showing the spatial distribution of the electron power deposition in a WTM (top) and CTTM (middle), for different injected electron energies (10, 20, 30, 40, 50, 100 keV). The ratio of WTM result to CTTM result is shown in the bottom panel. The shaded regions in the bottom panels show regions where the power is deposited at greater depths in the WTM compared to the CTTM (and hence ratio $\rightarrow\infty$). Dashed gray line: corona–-chromosphere boundary. Simulation set (a) uses a coronal temperature of $T = 20$ MK, coronal loop length of $L = 20''$, and a beamed injection.

Table 1
The Percentage of Available Nonthermal Electron Power Deposited in the Corona and Chromosphere for Set (a) Shown in Figure 4

Set (a)	CTTM		WTM ($T = 20$ MK)	
Energy (keV) (E/T)	Chromosphere (%)	Corona (%)	Chromosphere (%)	Corona (%)
10 (5.8)	0	100	61.1	38.9
20 (11.6)	0	100	21.3	78.7
30 (17.4)	5.3	94.7	31.7	68.3
40 (23.2)	64.2	35.8	63.7	36.3
50 (29.0)	80.7	19.3	79.6	20.4
100 (57.9)	*88.7*	*11.3*	*88.7*	*11.3*

Note. The 100 keV values are shown in italic since 100 keV electrons can travel further in this atmosphere than calculated within $\pm 30''$.

atmosphere type 1, using $n = 7 \times 10^{10}\,\mathrm{cm}^{-3}$ and $L = 20''$. The results are shown in Figure 6 (left) and Table 3. From the results of set (c), we find that:

1. For 30 keV electrons, the higher the temperature of the coronal plasma, the greater the fraction of nonthermal electron power transferred to the lower atmosphere, with less deposition in the corona (see Table 3). Electrons tend to a Maxwellian, and in higher coronal temperatures, thermalize at higher energies carrying a higher fraction of their power into the lower atmosphere. This dependence on coronal temperature is completely ignored in the CTTM.
2. Using atmosphere 1, at higher coronal temperatures, more power is deposited at greater depths in the lower atmosphere, and the ratio of WTM to CTTM deposition

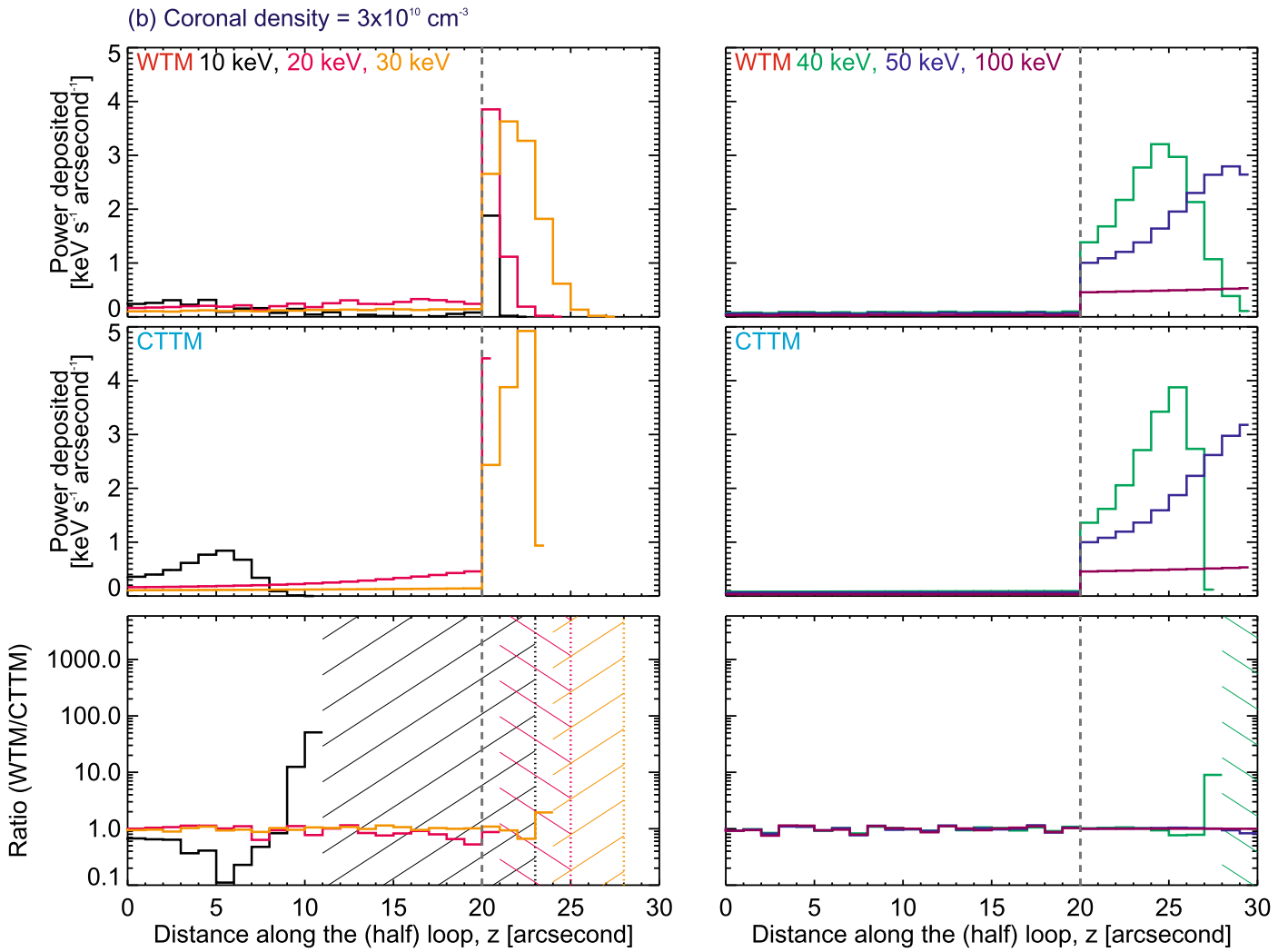

Figure 5. Lower density flaring corona. The results for (initially) monoenergetic simulation set (b) showing the spatial distribution of the electron power deposition in a WTM (top) and CTTM (middle), for different injected electron energies (10, 20, 30, 40, 50, 100 keV). The ratio of WTM result to CTTM result is shown in the bottom panel. The shaded regions in the bottom panels show regions where the power is deposited at greater depths in the WTM compared to the CTTM (and hence ratio $\rightarrow\infty$). Dashed gray line: corona–chromosphere boundary. Simulation set (b) uses a coronal temperature of $T = 20$ MK, coronal loop length of $L = 20''$, and a beamed injection.

Table 2
The Percentage of Available Nonthermal Electron Power Deposited in the Corona and Chromosphere for Set (b) Shown in Figure 5

Set (b)	CTTM		WTM ($T = 20$ MK)	
Energy (keV) (E/T)	Chromosphere (%)	Corona (%)	Chromosphere (%)	Corona (%)
10 (5.8)	0	100	46.8	53.2
20 (11.6)	48.3	51.7	55.6	44.4
30 (17.4)	83.8	16.2	83.6	16.4
40 (23.2)	91.5	8.5	91.5	8.5
50 (29.0)	93.5	6.5	93.5	6.5
100 (57.9)	*88.7*	*11.3*	*88.7*	*11.3*

Note. The 100 keV values are shown in italic since 100 keV electrons can travel further in this atmosphere than calculated within $\pm 30''$.

shows that at certain z in the lower atmosphere, more than three orders of magnitude more power can be deposited (see Figure 6, left). In the WTM, the decreased energy loss rate in the corona means that electrons carry more energy when they reach the chromospheric boundary and hence, they can travel deeper into the lower atmosphere.

3. It is possible that in high temperature plasma, if a fraction of the injected electrons have energies lower than $k_B T$, then the electrons will thermalize in the corona gaining energy and hence, deposit a higher fraction of energy in the lower atmosphere than suggested by their initial injected energy.

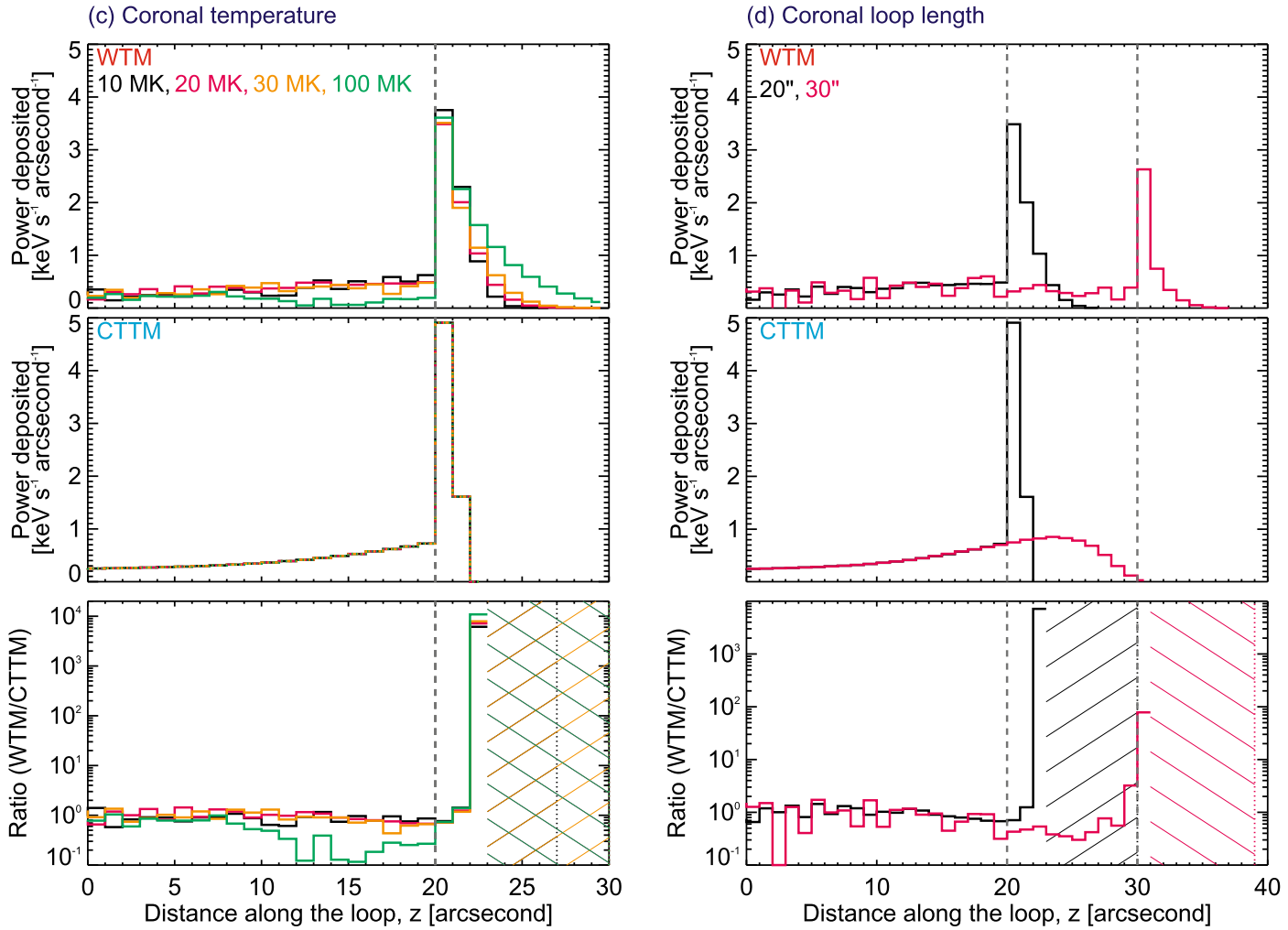

Figure 6. Left, different coronal temperatures; right, different coronal loop lengths. The results for the (initially) monoenergetic (30 keV) sets ((c); left) and ((d); right) showing the spatial distribution of deposition in a WTM (top) and CTTM (middle). Dashed gray line: corona–chromosphere boundary. Simulation sets (c) and (d) use a coronal density of: $n = 7 \times 10^{10}$ cm^{-3}, and a beamed injection. Set (c) uses a coronal loop length of $L = 20''$ and set (d) uses a coronal temperature of $T = 20$ MK. The ratio (WTM/CTTM) is shown in the bottom panel. The shaded regions in bottom panels show regions where the energy is deposited at greater depths in the WTM compared to the CTTM (and hence ratio $\rightarrow\infty$).

Table 3
The Percentage of Available Nonthermal Electron Power Deposited in the Corona and Chromosphere for Set (c) and Set (d) Shown in Figure 6

Set (c)	CTTM		WTM ($T = 20$ MK)	
Temperature (MK) ($E = 30$ keV$/T$)	Chromosphere (%)	Corona (%)	Chromosphere (%)	Corona (%)
10 (34.8)	47.1	52.9	51.8	48.2
20 (17.4)	47.1	52.9	50.7	49.3
30 (11.6)	47.1	52.9	53.5	46.5
100 (3.5)	47.1	52.9	76.6	23.4
Set (d)	CTTM		WTM ($T = 20$ MK)	
Half-loop Length ($''$) (E/T)	Chromosphere (%)	Corona (%)	Chromosphere (%)	Corona (%)
20 (17.4)	47.1	52.9	50.7	49.3
30 (17.4)	0.7	99.3	28.3	71.7

Set (d)—different coronal loop lengths: in set (d), we compare WTM and CTTM deposition in different loop lengths of $L = 20''$ and $L = 30''$. We inject beamed, monoenergetic electrons of 30 keV only into atmosphere type 1, using $n = 7 \times 10^{10}$ cm^{-3} and $T = 20$ MK. The results are shown in Figure 6 (right) and Table 3. From the results of set (d), we find that:

1. As expected, irrespective of the coronal loop length, more power is transferred to the lower atmosphere in the WTM compared to the CTTM. The larger the loop length (greater column depth), the greater time electrons spend in the corona and hence, more electrons tend toward Maxwellian or fully thermalize in the corona.

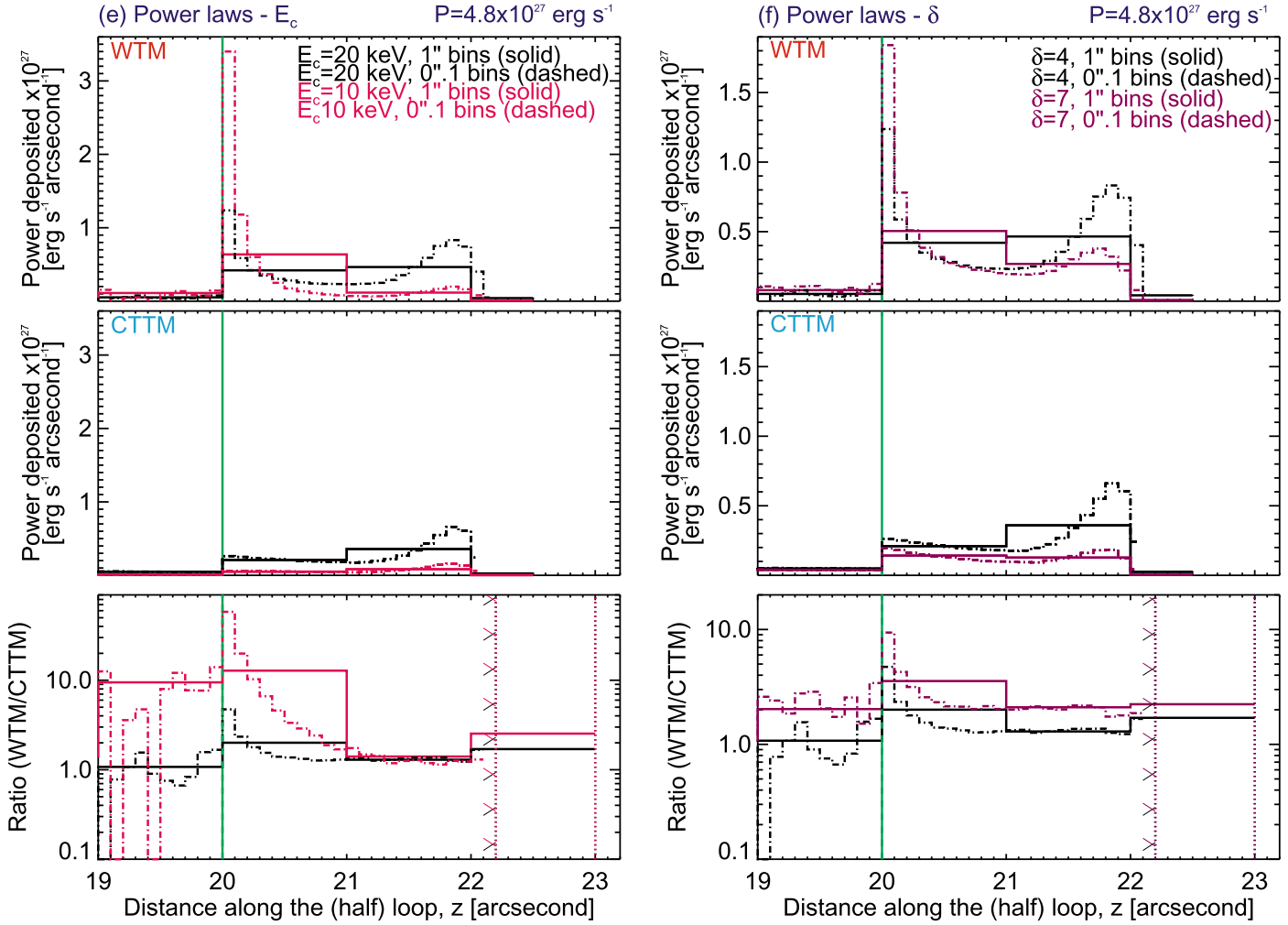

Figure 7. Power-law spectra: changes in electron power deposition with low-energy cutoff and spectral index. The results for sets ((e); left) and ((f); right) showing the spatial distribution of the electron power deposition (lower atmosphere only) in a WTM (top) and CTTM (middle). The ratio (WTM/CTTM) is shown in the bottom panel. Set (e) uses $E_c = 10$ keV and $E_c = 20$ keV and $\delta = 4$. Set (f) uses $\delta = 4$ and $\delta = 7$, with energies ranging between 20 and 50 keV. All runs have the same injected nonthermal electron power of $P = 4.8 \times 10^{27}$ erg s^{-1}. The shaded regions in the bottom panels show regions where the energy is deposited at greater depths in the WTM compared to the CTTM (and hence ratio $\rightarrow\infty$). Green line: corona–chromosphere boundary. Simulation sets (e) and (f) use atmosphere type 2 and coronal parameters of: $T = 20$ MK, $n = 7 \times 10^{10}$ cm^{-3}, and $L = 20''$.

Table 4
The Percentage of Available Nonthermal Electron Power Deposited in the Corona and Chromosphere for Set (e) and Set (f) Shown in Figure 7

Set (e; 1″ bins)	CTTM		WTM ($T = 20$ MK)	
E_c (keV) (E_c/T)	Chromosphere (%)	Corona (%)	Chromosphere (%)	Corona (%)
20 (11.6)	29.5	70.5	47.5	52.6
10 (5.8)	6.5	93.5	36.3	63.7
Set (f; 1″ bins)	**CTTM**		**WTM ($T = 20$ MK)**	
δ (keV) (E_c/T)	Chromosphere (%)	Corona (%)	Chromosphere (%)	Corona (%)
4 (11.6)	29.5	70.5	47.5	52.6
7 (11.6)	12.7	87.3	35.0	65.0

2. Although more power reaches the lower atmosphere in smaller loop lengths, the difference between the power transferred in the WTM and CTTM is greater for larger loop lengths. For example, for $L = 30''$, only 0.7% of the total nonthermal power is transferred in the CTTM, but in the WTM this rises to 28%. Further, the ratio of WTM/CTTM deposition at the chromospheric boundary is ∼100.

3.2. Monoenergetic Energy Inputs: Temporal Distribution of Deposited Power

In all simulation sets, we also determine how long it takes for all of the nonthermal electron power to be deposited in the flaring atmosphere. First, in Figure 8, we plot the results of sets (a) and (b). On each plot, we also add another simulation run where we inject (beamed) thermal electrons into the simulation.

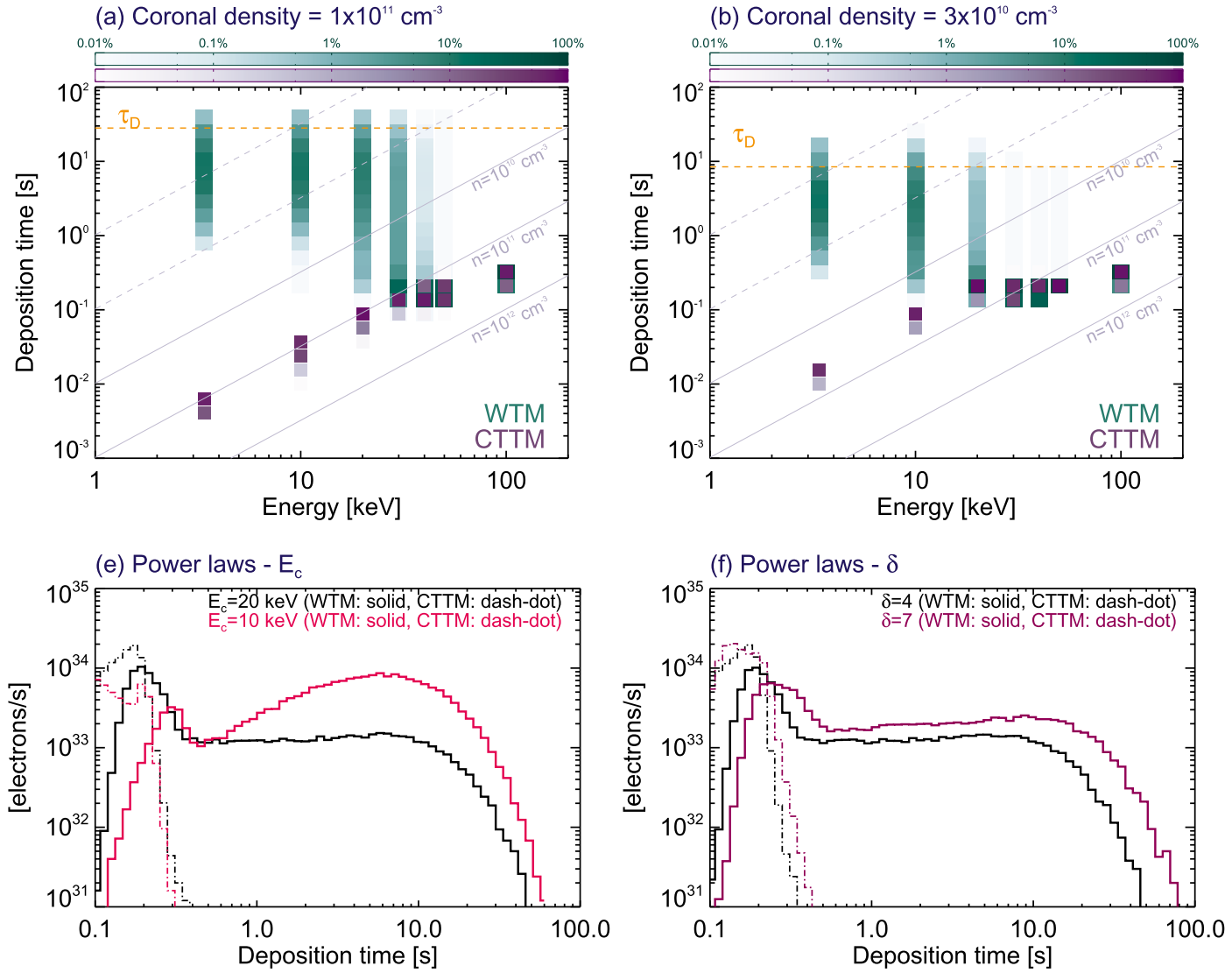

Figure 8. Top row: electron deposition times for simulation sets (a) and (b) (with the inclusion of thermal $2k_BT = 3.4$ keV electrons); color bar indicates (e/s), for electrons in a WTM (green) and CTTM (purple). In a WTM, low-energy electrons that thermalize in the corona reach and deposit their energy in the chromosphere over longer timescales of second to tens of seconds. Orange line: τ_D = thermal diffusion time. Purple lines: analytic energy loss times in a CTTM for a given density. Middle and bottom rows: electron deposition times for selected simulation sets (e) and (f). The shape of the delayed deposition curves is dependent on both the properties of the nonthermal electrons and coronal plasma properties.

Note that in the simulations, the injected electrons relax to the flux-averaged mean energy $2k_BT$ of the background plasma, and a $T = 20$ MK corona gives $2k_BT = 3.4$ keV. Figure 7 shows that in a WTM, lower energy electrons $E/k_BT \leqslant 11.6$ can deposit their power in the lower atmosphere over a large range of timescales, and as expected the WTM result tends to the CTTM result when $E > 50$ keV. These timescales are shown in Figure 8 for both $n = 1 \times 10^{11}$ cm^{-3} and $n = 3 \times 10^{10}$ cm^{-3} cases. In the WTM, many electrons still deposit their power at times close to CTTM values, and WTM times converge to CTTM times as the electron energy increases. However, in the WTM, lower energy electrons show a large tail of delayed deposition in the lower atmosphere (of seconds to tens of seconds), unaccounted for in the CTTM, due to partially and fully thermalized electrons.

As an illustrative example from Figure 8, a 10 keV electron will thermalize quickly in a high density corona ($n = 10^{11}$ cm^{-3}) over a distance of $<10''$ (over a time of <0.1 s). In the CTTM, 10 keV electrons in this scenario never reach the chromosphere and deposit energy. However, in a WTM, once a 10 keV electron has thermalized, it could travel hundreds of arcseconds in a random walk, in the hot coronal region, before exiting into the cooler and denser chromosphere. Therefore, depending on their path (the amount of scattering) and thermalization time, electrons can now exit the corona over a range of timescales from subsecond to tens of seconds.[3]

3.3. Isotropic Injection

For cases where we input an isotropic electron distribution, we find similar results: more energy is deposited in the lower atmosphere in the WTM than in a CTTM. For example, in one simulation where we inject 30 keV electrons into a corona ($T = 20$ MK, $n = 7 \times 10^{10}$ (cm^{-3}) and $L = 20''$), independent of whether the injected electron distribution is beamed or isotropic, more energy is deposited at deeper locations in the

[3] These times will be even further affected by turbulent scattering in the corona.

lower atmosphere in a WTM than in a CTTM, up to 1000 times more in the beamed case, at certain locations, and up to 4 times in the isotropic case. Moreover, initially isotropic nonthermal distributions deposit energy over a greater range of timescales, and more energy is deposited at greater times relative to a beamed injection of electrons, possibly providing a diagnostic of electron anisotropy.

3.4. Solar Flare Power-law Energy Inputs

To investigate how the power of flare-accelerated electrons is transferred and deposited in a more realistic solar or stellar flare scenario, we also perform simulation runs using an injected electron power-law energy distribution of the form $F(E_0) \sim E_0^{-\delta}$ (set (e): different E_c and set (f): different δ). In these runs, we use the following plasma parameters and injected electron inputs: $T = 20$ MK, $n = 7 \times 10^{10}\,\mathrm{cm}^{-3}$, and the more realistic atmosphere type 2. Each electron distribution has a total power of $P = 4.8 \times 10^{27}\,\mathrm{erg\,s}^{-1}$, with spectral index $\delta = 4$ or $\delta = 7$, a low-energy cutoff of $E_c = 10$ keV or $E_c = 20$ keV, and a high-energy cutoff of $E_H = 50$ keV. Again, such a low high-energy cutoff is used since we want to examine low-energy electrons that are incorrectly modeled by the CTTM. The results are shown in Figure 7 and Table 4.

For the power-law energy inputs we find the following notable results:

1. As expected, the differences in CTTM and WTM power deposition follow the results of Sections 3.1 and 3.2.
2. For a given injected electron power, we see a larger difference in CTTM and WTM deposition for electron distributions with a smaller low-energy cutoff E_c. Spatially, more power is deposited at greater depths and up to 12 times more power can be deposited in the lower atmosphere for $E_c = 10$ keV and 2 times more energy for $E_c = 20$ keV, at a given location, for the studied conditions.
3. For a given injected electron power, we see a larger difference in CTTM and WTM deposition for electron distributions with softer spectral indices. Spatially, more power is deposited at greater depths and up to 4 times more power can be deposited in the lower atmosphere for $\delta = 7$ and up to 2 times for $\delta = 4$, at a given location, for the studied conditions.
4. The simulation runs using $0\farcs1$ binning show that thermalized low-energy electrons deposit a large fraction of power at the top of the chromospheric boundary.
5. Electron power-law distributions with a higher fraction of low-energy electrons (i.e., smaller E_c or larger δ), that partially or fully thermalize in the corona, deposit more of their energy at greater times (second to tens of second timescales).

4. Discussion

In this work, we show that the CTTM does not adequately approximate the transport and deposition of energetic electrons in flaring, and therefore strongly heated, solar, or stellar atmospheres. In the CTTM, neglecting second order effects such as velocity diffusion leads to an underestimate of the energy transferred to the low atmosphere in the majority of cases, especially by lower energy electrons with $E < 50$ keV (or equivalently $E/k_BT \leqslant 20$) that can fully or partially thermalize in the flaring corona and transfer energy diffusively. This leads to a difference in the spatial distribution of deposited nonthermal electron power in both the corona and cool layers of the low atmosphere. Understanding energy transfer by low-energy electrons is important. Most solar flare nonthermal electron distributions are consistent with steeply decreasing power laws with the bulk of the power held by electrons with $E < 50$ keV. Further, the thermalization of nonthermal electrons in the corona leads to the nonthermal electron power being deposited over a large range of times from subsecond to tens of second, producing delayed heating in the lower atmosphere. The temporal distribution of this heating profile could act as a diagnostic of both nonthermal electron properties (even electron anisotropy, since isotropic electrons will spend longer in the coronal plasma, leading to greater thermalization), and the plasma conditions in the corona (temperature, number density, and the extent of hot coronal plasma), if it can be extracted from observation. Using a full WTM description of energy transfer and deposition may be especially important for the analysis of stellar flares with higher coronal temperatures and densities. Also, the WTM description of energy deposition may be important for the study of microflares with low-energy $\leqslant$10 keV accelerated electrons (e.g., Wright et al. 2017) that can easily thermalize in the coronal plasma, but still produce heating in the lower atmosphere.

The development of the WTM shows the important role coronal plasma properties play in determining the acceleration, transport, and now deposition of flare-accelerated nonthermal electron power. Future X-ray observatories must aim to better constrain the plasma properties for this purpose. These simulation results, although applicable to archived *RHESSI* data, anticipate the launch of direct imaging X-ray missions, that will be able to provide a more detailed picture of the solar flare environment (temperature, density, "hot" plasma extent) in different regions of the flare, using better spatial and temporal resolution, high dynamic range, and greater imaging spectroscopy capabilities. The delayed energy transfer by thermalized electrons should be observable by imaging low-energy soft X-rays (<5 keV). Current high spectral, spatial and temporal observations with *Interface Region Imaging Spectrograph* (De Pontieu et al. 2014) in the transition region and chromosphere can be used to study the effects of delayed heating by partially or fully thermalized nonthermal electron distributions.

Jeffrey et al. (2015) showed that the flaring corona is made up of multiple loops of varying temperature and density. These varying plasma parameters have a huge effect on both the injected electron parameters and on the resulting energy deposition. Such variation must be taken into account in future modeling. Further, we must study a changing, dynamic atmosphere, since deposition by thermalized nonthermal electrons is modulated by changes in the coronal plasma properties. Importantly, we suggest that hydrodynamic models that use the CTTM approximation as an input should be reevaluated, and eventually the WTM should replace any CTTM approximations. WTM energy deposition with the inclusion of extended loop turbulence and magnetic trapping will also be the subject of upcoming work. As stated, the appeal of the CTTM is its simple analytic form and the next step is to produce a semianalytic WTM function that can be used by both the solar and stellar communities to determine the deposition of energy in flaring atmospheres.

N.L.S.J., E.P.K., and L.F. gratefully acknowledge the financial support from the Science and Technology Facilities Council (STFC) Consolidated Grant ST/P000533/1. The work is supported by an international team grant ("Solar flare acceleration signatures and their connection to solar energetic particles" http://www.issibern.ch/teams/solflareconnectsolenerg/) from the International Space Sciences Institute (ISSI) Bern, Switzerland.

ORCID iDs

Natasha L. S. Jeffrey https://orcid.org/0000-0001-6583-1989
Eduard P. Kontar https://orcid.org/0000-0002-8078-0902
Lyndsay Fletcher https://orcid.org/0000-0001-9315-7899

References

Acton, L. W., Leibacher, J. W., Canfield, R. C., et al. 1982, ApJ, 263, 409
Alaoui, M., & Holman, G. D. 2017, ApJ, 851, 78
Aschwanden, M. J., Boerner, P., Ryan, D., et al. 2015, ApJ, 802, 53
Aschwanden, M. J., Brown, J. C., & Kontar, E. P. 2002, SoPh, 210, 383
Aschwanden, M. J., Bynum, R. M., Kosugi, T., Hudson, H. S., & Schwartz, R. A. 1997, ApJ, 487, 936
Aschwanden, M. J., Caspi, A., Cohen, C. M. S., et al. 2017, ApJ, 836, 17
Aschwanden, M. J., Stern, R. A., & Güdel, M. 2008, ApJ, 672, 659
Battaglia, M., Kontar, E. P., Fletcher, L., & MacKinnon, A. L. 2012, ApJ, 752, 4
Benz, A. O. 2008, LRSP, 5, 1
Bespalov, P. A., Zaitsev, V. V., & Stepanov, A. V. 1991, ApJ, 374, 369
Brown, J. C. 1971, SoPh, 18, 489
Brown, J. C., Turkmani, R., Kontar, E. P., MacKinnon, A. L., & Vlahos, L. 2009, A&A, 508, 993
Casadei, D., Jeffrey, N. L. S., & Kontar, E. P. 2017, A&A, 606, A2
Caspi, A., Krucker, S., & Lin, R. P. 2014, ApJ, 781, 43
Culhane, J. L., Vesecky, J. F., & Phillips, K. J. H. 1970, SoPh, 15, 394
De Pontieu, B., Title, A. M., Lemen, J. R., et al. 2014, SoPh, 289, 2733
Emslie, A. G. 1978, ApJ, 224, 241
Emslie, A. G. 1980, ApJ, 235, 1055
Emslie, A. G. 2003, ApJL, 595, L119
Emslie, A. G., Dennis, B. R., Shih, A. Y., et al. 2012, ApJ, 759, 71
Emslie, A. G., & Smith, D. F. 1984, ApJ, 279, 882
Emslie, A. G., & Sturrock, P. A. 1982, SoPh, 80, 99
Fletcher, L., Dennis, B. R., Hudson, H. S., et al. 2011, SSRv, 159, 19
Fletcher, L., & Hudson, H. S. 2008, ApJ, 675, 1645
Galloway, R. K., MacKinnon, A. L., Kontar, E. P., & Helander, P. 2005, A&A, 438, 1107
Gardiner, C. W. 1986, ApOpt, 25, 3145
Gordovskyy, M., & Browning, P. K. 2012, SoPh, 277, 299
Gordovskyy, M., Browning, P. K., Kontar, E. P., & Bian, N. H. 2014, A&A, 561, A72
Guo, J., Emslie, A. G., Kontar, E. P., et al. 2012, A&A, 543, A53
Hannah, I. G., Kontar, E. P., & Sirenko, O. K. 2009, ApJL, 707, L45
Hirayama, T. 1974, SoPh, 34, 323
Holman, G. D., Aschwanden, M. J., Aurass, H., et al. 2011, SSRv, 159, 107
Hoyng, P., Duijveman, A., Machado, M. E., et al. 1981, ApJL, 246, L155
Jeffrey, N. L. S., Fletcher, L., Labrosse, N., & Simões, P. J. A. 2018, SciA, 4, 2749
Jeffrey, N. L. S., & Kontar, E. P. 2013, ApJ, 766, 75
Jeffrey, N. L. S., Kontar, E. P., Bian, N. H., & Emslie, A. G. 2014, ApJ, 787, 86
Jeffrey, N. L. S., Kontar, E. P., & Dennis, B. R. 2015, A&A, 584, A89
Karney, C. 1986, CoPhR, 4, 183
Knight, J. W., & Sturrock, P. A. 1977, ApJ, 218, 306
Kolmogorov, A. 1931, MatAn, 104, 415
Kontar, E. P., Bian, N. H., Emslie, A. G., & Vilmer, N. 2014, ApJ, 780, 176
Kontar, E. P., Brown, J. C., Emslie, A. G., et al. 2011a, SSRv, 159, 301
Kontar, E. P., Emslie, A. G., Massone, A. M., et al. 2007, ApJ, 670, 857
Kontar, E. P., Hannah, I. G., & Bian, N. H. 2011b, ApJL, 730, L22
Kontar, E. P., Hannah, I. G., Jeffrey, N. L. S., & Battaglia, M. 2010, ApJ, 717, 250
Kontar, E. P., Jeffrey, N. L. S., & Emslie, A. G. 2019, ApJ, 871, 225
Kontar, E. P., Jeffrey, N. L. S., Emslie, A. G., & Bian, N. H. 2015, ApJ, 809, 35
Kontar, E. P., Perez, J. E., Harra, L. K., et al. 2017, PhRvL, 118, 155101
Kretzschmar, M. 2011, A&A, 530, A84
Larosa, T. N., & Moore, R. L. 1993, ApJ, 418, 912
Lemons, D. S., Winske, D., Daughton, W., & Albright, B. 2009, JCoPh, 228, 1391
Lifshitz, E. M., & Pitaevskii, L. P. 1981, Physical Kinetics (Oxford: Pergamon)
Lin, R. P., Dennis, B. R., Hurford, G. J., et al. 2002, SoPh, 210, 3
McClements, K. G. 1987, A&A, 175, 255
Parker, E. N. 1957, JGR, 62, 509
Petrosian, V. 2012, SSRv, 173, 535
Priest, E., & Forbes, T. 2000, Magnetic Reconnection (Cambridge: Cambridge Univ. Press)
Somov, B. V. 2007, Coulomb Collisions in Astrophysical Plasma (New York: Springer), 133, doi:10.1007/978-0-387-68894-7_9
Spitzer, L. 1962, Physics of Fully Ionized Gases (New York: Interscience)
Stepanov, A. V., Yokoyama, T., Shibasaki, K., & Melnikov, V. F. 2007, A&A, 465, 613
Strauss, R. D. T., & Effenberger, F. 2017, SSRv, 212, 151
Sturrock, P. A. 1973, NASSP, 342, 3
Sweet, P. A. 1958, in IAU Symp. 6, Electromagnetic Phenomena in Cosmical Physics, ed. B. Lehnert (Cambridge: Cambridge Univ. Press), 123
Syrovatskii, S. I., & Shmeleva, O. P. 1972, SvA, 16, 273
Tsuneta, S., Acton, L., Bruner, M., et al. 1991, SoPh, 136, 37
Vernazza, J. E., Avrett, E. H., & Loeser, R. 1981, ApJS, 45, 635
Veronig, A. M., & Brown, J. C. 2004, ApJL, 603, L117
Vlahos, L., & Papadopoulos, K. 1979, ApJ, 233, 717
Vlahos, L., Pisokas, T., Isliker, H., Tsiolis, V., & Anastasiadis, A. 2016, ApJL, 827, L3
Warmuth, A., & Mann, G. 2016, A&A, 588, A116
Woods, T. N., Kopp, G., & Chamberlin, P. C. 2006, JGRA, 111, A10S14
Wright, P. J., Hannah, I. G., Grefenstette, B. W., et al. 2017, ApJ, 844, 132
Xu, Y., Emslie, A. G., & Hurford, G. J. 2008, ApJ, 673, 576
Zharkova, V. V., & Gordovskyy, M. 2006, ApJ, 651, 553